

1 Exploring Mechanisms of Variability and Predictability  
2 of Atlantic Meridional Overturning Circulation in Two  
3 Coupled Climate Models

4 ROSS TULLOCH \* AND JOHN MARSHALL \*

*Department of Earth, Atmospheric and Planetary Sciences,*

*Massachusetts Institute of Technology, 77 Massachusetts Avenue, Cambridge, MA*

5 November 22, 2011

6 **Abstract**

7 Multi-decadal variability in the Atlantic Meridional Overturning Circulation (AMOC)  
8 of the ocean is diagnosed in the NCAR Community Climate System Model (CCSM3)  
9 and the GFDL Coupled Model (CM2.1). Common diagnostic approaches are applied  
10 to draw out similarities and differences between the two models. An index of AMOC

---

*\*Corresponding authors' addresses:*

Ross Tulloch, Department of Earth, Atmospheric and Planetary Sciences, Massachusetts Institute of Technology, 77  
Massachusetts Avenue, Cambridge MA 02139. E-mail: tulloch@mit.edu

John Marshall, Department of Earth, Atmospheric and Planetary Sciences, Massachusetts Institute of Technology, 77  
Massachusetts Avenue, Cambridge MA 02139. E-mail: jmarsh@mit.edu

11 variability is defined and the manner in which key variables covary with it is deter-  
12 mined. In both models it is found that: (i) AMOC variability is associated with upper  
13 ocean (top 1 km) density anomalies (dominated by temperature) on the western mar-  
14 gin of the basin in the region of the Mann Eddy with a period of about 20 years.  
15 These anomalies modulate the trajectory and strength of the North Atlantic Current.  
16 The importance of the western margin is a direct consequence of the thermal wind  
17 relation and is independent of the mechanisms that create those density anomalies.(ii)  
18 Density anomalies in this key region are part of a larger-scale pattern that propagates  
19 around the subpolar gyre and acts as a ‘pacemaker’ of AMOC variability. (iii) The  
20 observed variability is consistent with the primary driving mechanism being stochas-  
21 tic wind-curl forcing, with Labrador Sea convection playing a secondary role. Finally,  
22 ‘toy models’ of delayed oscillator form are fitted to power spectra of key variables and  
23 used to infer “quality factors” (Q-factors), which characterize the bandwidth relative  
24 to the center frequency and hence AMOC predictability horizons. The two models  
25 studied here have Q-factors of around 2, suggesting that prediction is possible out to  
26 about two cycles, which is likely larger than the real AMOC.

## 27 **1. Introduction**

28 The Atlantic Meridional Overturning Circulation of the ocean (AMOC) plays a central role in cli-  
29 mate, transporting heat across the equator in to the North Atlantic basin. It is thought to modulate,  
30 for example, sea surface temperature (SST) and mediate sea ice extent in high northern latitudes  
31 (Kushnir 1994; Mahajan et al. 2011a). The AMOC in coupled climate models often exhibits pro-

32 nounced decadal variability that might be reflected in, and inherited by, other parts of climate  
33 system. Moreover, if decadal AMOC variability is associated with slow ocean processes which  
34 are predictable, then such predictability (if it exists) might be leveraged and exploited in coupled  
35 climate models used for climate change prediction and attribution — see Leetmaa and Marshall  
36 (2006); Hurrell et al. (2006) for a background discussion.

37 Currently there is intense interest in understanding the AMOC, documenting how it varies in  
38 observations (Kushnir 1994; Delworth and Mann 2000; Johns et al. 2011) and in models (Weaver  
39 et al. 1993; Delworth et al. 1993; Griffies and Tziperman 1995; Jayne and Marotzke 2001; Dai  
40 et al. 2005; Dong and Sutton 2005; Jungclaus et al. 2005; Danabasoglu 2008; Tziperman et al.  
41 2008; Hawkins and Sutton 2009), and identifying the causes of that variability. Thus far it has  
42 not been possible to unambiguously identify a single driving mechanism and indeed there seems  
43 to be much model dependence in AMOC variability — see Marshall et al. (2001); Danabasoglu  
44 (2008); Yoshimori et al. (2010); Kwon and Frankignoul (2011); Sévellec and Fedorov (2011, and  
45 references therein).

46 AMOC variability diagnosed in models typically falls into one of the following types:

- 47 1. self-sustained internal (ocean-only) oscillations (Colin de Verdière and Huck 1999; Te Raa  
48 et al. 2004; Zhu and Jungclaus 2008; Buckley 2011).
- 49 2. a damped oceanic mode stochastically-excited by the atmosphere (Delworth et al. 1993;  
50 Griffies and Tziperman 1995; Delworth and Greatbatch 2000; Dai et al. 2005; Dong and  
51 Sutton 2005; Sévellec and Fedorov 2011; Frankcombe et al. 2009) and/or freshwater inter-  
52 actions with the Arctic (Jungclaus et al. 2005; Delworth et al. 1997; Olsen et al. 2008).
- 53 3. coupled atmosphere-ocean modes (Weaver and Valcke 1998; Eden and Willebrand 2001;

54 Oka and Hasumi 2006)

55 Some of the present uncertainty reflects the undoubted complexity of the processes at work.  
56 However, this is compounded by the fact that different diagnostic methods are employed by differ-  
57 ent investigators who come to the problem with differing viewpoints. Here we attempt to rational-  
58 ize the situation somewhat. In Section 2 we diagnose AMOC variability in two different coupled  
59 climate models — the NCAR Community Climate System Model 3 (CCSM3) and the GFDL Cou-  
60 pled Model 2.1 (CM2.1). An index of AMOC variability is defined and the manner in which key  
61 variables covary with it is used to draw out aspects of underlying mechanisms and similarities and  
62 differences between the two models. We draw attention to the role of subsurface density anomalies  
63 that abut the continental shelf on the western margin of the Atlantic basin in the region of the Mann  
64 Eddy. This region is located at the latitude at which the mean AMOC is a maximum and where it  
65 exhibits maximum variability in the two models. In Section 3 we fit ‘toy models’ of delayed oscil-  
66 lator form to observed spectra of key variables and use them to infer ‘Q-factors’, characterizing the  
67 bandwidth relative to the center frequency, and hence AMOC predictability horizons. Finally, in  
68 Section 4, we conclude, drawing out aspects that might pertain to the real, rather than the modeled,  
69 ocean.

## 70 **2. Variability in the Atlantic Ocean in two coupled climate mod-** 71 **els**

72 Here we explore the variability of Atlantic Meridional Overturning Circulation (hereafter AMOC)  
73 in 500-year control integrations of the NCAR Community Climate System Model 3 (CCSM3) and

74 the GFDL Coupled Model 2.1 (CM2.1). The detailed configurations of each model are described  
75 in Appendix A. AMOC variability has been studied before in these two models, as we now briefly  
76 describe.

77 In Danabasoglu (2008), deep convection in the Labrador Sea region was identified as a key pre-  
78 cursor to decadal AMOC variability in CCSM3, and complicated interactions between the MOC  
79 and deep water formation, the North Atlantic Oscillation and the subpolar gyre circulation are  
80 identified as drivers of MOC variability. Yoshimori et al. (2010) analyzed a low resolution version  
81 of CCSM3 and argued that variability involves an interaction between advection of salt and surface  
82 density in the subpolar gyre, with a connection to the North Atlantic Oscillation (NAO). A positive  
83 feedback involving eddy activity in the atmosphere was invoked. Meanwhile, Kwon and Frankig-  
84 noul (2011) identified regimes of high and low AMOC variability in CCSM3. The first regime  
85 (studied by Danabasoglu 2008) has a very regular 20 year oscillation and the second regime has  
86 red noise-like variability. They concluded that the variability in the second regime could be under-  
87 stood as a damped oceanic mode that is stochastically-excited by the NAO. They also noted that  
88 a delayed positive feedback caused by changes in horizontal ocean circulation increased AMOC  
89 persistence from 5 to 10 years.

90 Zhang (2008) noted that AMOC variability in CM2.1 is associated with a dipole in subsurface  
91 temperature anomalies. A positive AMOC is associated with negative temperature anomalies in the  
92 Gulf Stream region and slightly weaker positive temperature anomalies in the subpolar gyre, indi-  
93 cating that a strengthening of the AMOC in CM2.1 is associated with a weakening of the subpolar  
94 gyre. Zhang et al. (2011) argued that North Brazil Current transport lags Labrador Sea convection  
95 in CM2.1 and is a useful indicator for AMOC variability. These two studies imply that freshwater  
96 fluxes likely play a role in generating AMOC variability. On the other hand, Frankcombe et al.

97 (2009) argued that the dominant timescale of North Atlantic variability in CM2.1 is determined  
98 by the time for subsurface temperature anomalies to propagate westwards as baroclinic Rossby  
99 waves.

100 Results from previous studies on CCSM3 and CM2.1 indicate that a number of factors may  
101 affect AMOC variability, and that there is no single underlying mechanism across models. The  
102 prevailing view appears to be that AMOC variability is excited by external NAO forcing in CCSM3  
103 and freshwater fluxes in CM2.1. Thus far there has been little attempt to draw parallels between  
104 the two models and identify common driving mechanisms in them. This is the goal of the present  
105 study. We argue that, in both models, density anomalies are created in the subpolar gyre and affect  
106 AMOC via the thermal wind relation upon reaching the western boundary.

107 We begin by defining an index of MOC variability and go on to study how other aspects of the  
108 circulation, such as temperature ( $T$ ), salinity ( $S$ ) and potential density ( $\rho$ ) anomalies, covary with  
109 it. Much use is made of composite property maps defined at various leads and lags referenced to  
110 a (HI)-(LO) MOC index, which is defined in Section 2a. Emphasis is placed on density anomalies  
111 on the western margin of the gyre in the region of the Grand Banks, which play a key role in  
112 pacing MOC variability in both models. We conclude the section by drawing together aspects of  
113 the variability that are common between the two models. This is used to motivate the construction  
114 of simplified ‘toy models’ described in Section 3.

115 **2a. MOC Variability**

116 Fig. 1(a,d) shows contours of the time averaged MOC (in Sv) in CCSM3 and CM2.1.<sup>1</sup> In both  
 117 models the maximum overturning occurs just north of 40°N at a depth of roughly 1 km. Time  
 118 series of annual-mean MOC averaged over the regions indicated by the black box (roughly from  
 119 35° to 50° and 1800 m to 500 m depth) in each model are shown in Fig. 1(b,e). Years that are more  
 120 than one standard deviation above (below) the mean are marked with x's (squares). These years  
 121 will now be used to create composite variables based on a (HI)-(LO) MOC index, *i.e.*, composites  
 122 are the average of a given variable over years when the MOC is (HI) minus the average when the  
 123 MOC is (LO). This technique was used, for example, in Czaja and Marshall (2001) to study the  
 124 evolution of SST anomalies in the Atlantic based on an SST dipole index.

125 The (HI)-(LO) MOC pattern is shown in Fig. 1(c,f). It has a maximum magnitude of 6.8 Sv  
 126 in CCSM3 and 4.6 Sv in CM2.1 and is located near the black box at zero lag. The patterns are  
 127 slightly deeper than the mean MOC, which is consistent with the first empirical orthogonal function  
 128 (EOF1) (see Danabasoglu 2008).

129 **2b. Covarying temperature signals**

130 Figs. 2(a,d) show power spectra of the MOC indices (red lines) in Fig. 1 for both CCSM3 and  
 131 CM2.1. Also plotted are power spectra of a temperature index ( $T$ ), defined as the upper 1 km tem-  
 132 perature averaged over the gray-boxed region near the Grand Banks in Figs. 2(b,c,e,f). The gray

---

<sup>1</sup>Only the explicitly calculated, Eulerian component of the MOC is considered here, as in Danabasoglu (2008). In  
 CM2.1, the parameterized bolus contribution has a negligible effect on the MOC spectrum since its variance is less  
 than 1% of the Eulerian contribution.

133 shading indicates 95% confidence limits of the MOC for a  $\chi^2$  distribution. The significance of this  
 134 boxed region will become more clear in Sections 2d and 2e below. In both models, peaks in vari-  
 135 ability are evident at approximately 20 years. Notice that the spectral content of the MOC-index  
 136 and the  $T$ -index are very similar, indicating that the MOC and  $T$  indices are varying together,  
 137 with perhaps a delay between them. The green lines show  $\omega^{-2}$  power laws: on subdecadal time-  
 138 scales the  $T$  signal is likely to be integrating a white noise process, consistent with Frankignoul  
 139 and Müller (1979). Later, in Section 3, we will model the decadal peak as a delayed oscillator  
 140 using ideas in Marshall et al. (2001).

141 Figs. 2(b,e) show composite maps of  $T$  based on the (HI)-(LO) MOC index defined in Fig. 1.  
 142 Regions where the (HI)-(LO) composites are not statistically significant at the 95% confidence  
 143 level with the two-tailed Student's t-test are shaded white. Note that the temporal degrees of  
 144 freedom are estimated using Effective Sample Size diagnostic of Bretherton et al. (1999). The  
 145 spatial patterns of  $T$  at years with high MOC minus  $T$  in years with low MOC closely matches the  
 146 first Empirical Orthogonal Function (EOF1) of  $T$  shown in Figs. 2(c,f). Thus the primary mode of  
 147 variability in  $T$  is nearly in phase with MOC. Cross-correlation analysis, not shown, reveals that  
 148 (minus) the boxed  $T$ -index lags MOC by 2 years in CCSM3, with cross-correlation of about 0.47  
 149 (compared to a 95% confidence level of about 0.2), while in CM2.1 the  $T$ -index is in phase with  
 150 MOC with correlation 0.7 (compared to a 95% confidence level of about 0.185). As described in  
 151 Section 2f, the  $T$ -index delay in CCSM3 is likely due to deep convection in the Labrador Sea,  
 152 which provides a slow pathway for subsurface density anomalies near 1 km depth to reach the  
 153 Grand Banks region.

154 In both models, most of the variability of the MOC-index is associated with temperature dom-  
 155 inated density anomalies on the western boundary near the Grand Banks, *i.e.*, the blue regions



156 within the gray boxes in Fig. 2, which will be described in more detail in Section 2d. The black  
157 contours in Figs. 2(b,c,e,f) indicate the time-mean zero wind stress curl lines, roughly marking the  
158 gyre boundaries. The close correspondence between the maximum temperature variations and the  
159 zero-wind stress curl line is indicative of a possible role of wind forcing, because the greatest part  
160 of the wind stress curl variability lies along the zero wind stress curl line.

### 161 **2c. Covarying density signals**

162 Fig. 3 shows composite maps of potential density averaged over the top 1 km using the (HI)-(LO)  
163 MOC index in CCSM3. Fig. 3(b) is computed by subtracting the high-index composite from the  
164 low-index composite. The (HI)-(LO) map in Fig. 3(b) is very similar to the map in Fig. 2(b) (but  
165 with opposite sign), indicating that density anomalies at high and low MOC states are dominated  
166 by temperature anomalies. The corresponding (HI)-(LO) salt map (not shown) has very similar  
167 patterns and signs as Fig. 2(b), showing that  $T$  and  $S$  are compensated, except in the Labrador Sea  
168 region (as noted by Danabasoglu 2008). The most pronounced feature of the density pattern (blue  
169 region in Fig. 3b) forms near the zero wind stress curl line and the mid-Atlantic ridge. The ‘5 years  
170 earlier’ map in Fig. 3(a) is obtained by taking the average of (HI – 5) years minus the average  
171 of (LO – 5) years. It shows advection of a positive density anomaly around the subpolar gyre.  
172 The ‘5 years later’ map in Fig. 3(d) shows the opposite phase, with a negative density anomaly  
173 beginning to advect cyclonically around the subpolar gyre. Also, the positive density anomaly that  
174 previously propagated around the subpolar gyre has merged with another positive density anomaly  
175 that formed in-situ off of the Grand Banks (*i.e.*, inside the boxed region in Fig. 3b). This merging  
176 of positive density anomalies is also visible in the meridional section shown in Fig. 5(c). Labrador

177 Sea anomalies subduct and propagate southward before merging with a shallower density anomaly  
178 in the Grand Banks region.

179 Fig. 4 shows maps of potential density based on the composite (HI)-(LO) MOC index in  
180 CM2.1, analogous to Fig. 3 for CCSM3. In CM2.1, as in CCSM3, the composite density map  
181 at 0 years (Fig. 4b) closely matches the composite temperature map in Fig. 2(d): Temperature  
182 dominates, with salinity compensating (not shown) everywhere except in the region of deep con-  
183 vection in the Labrador Sea, where salt anomalies dominate at 0 lag. Again, the largest density  
184 anomalies are found along the zero wind stress curl line, but they originate further north near the  
185 mid-Atlantic ridge and propagate both west into the Labrador Sea and southwest into the region  
186 off the Grand Banks.

## 187 **2d.** *Role of density anomalies on the western boundary*

188 Buckley (2011) showed that MOC variability occurs almost entirely on the western boundary in  
189 coupled aqua-planet simulations with meridional continental barriers. In one of their model con-  
190 figurations, with flat bottom bathymetry, anomalies generated near the eastern boundary propagate  
191 westward and trigger MOC variations when they reach the western boundary, in accord with the  
192 thermal wind relation. The temperature anomalies shown in Fig. 2 form in different locations in  
193 the two more realistic models studied here, but all models suggest that density anomalies propagate  
194 around the subpolar gyre and influence the MOC when they reach the western boundary.

195 Here, motivated by that study, we investigate the role of density anomalies on the western  
196 boundary and their association with MOC anomalies. Fig. 5 shows composites of zonal and merid-  
197 ional cross-sections of meridional velocity and density in CCSM3 (top row) and CM2.1 (bottom

row), from the regions indicated by the gray dashed lines in panel d of Figs. 3 and 4. The zonal cross-sections are averaged from 40°N to 45°N, which is approximately the latitude range where the MOC is largest. The meridional cross-sections are averaged from 50°W to 40°W, encompassing the longitude where the deep western boundary current flows offshore of the Grand Banks and where density anomalies associated with MOC variability are found. Fig. 5(a) shows that the largest transport differences between high and low MOC years occurs around 40°W, where both the Gulf Stream and the deep western boundary current are anomalously strong. The tripole pattern of meridional velocity in Fig. 5(a) is consistent with the density dipole present in the zonal section of Fig. 5(b). However, as is evident from a consideration of the thermal wind equation (see below) the positive density anomaly on the western boundary is associated with the major part of MOC variability.

The bottom row of Fig. 5 shows zonal and meridional composite cross-sections of meridional velocity and density in CM2.1, averaged over the same latitude and longitude bands. Analogously to CCSM3, the transport anomalies in Fig. 5(d) are centered over 40°W and are a maximum when the Gulf Stream and deep western boundary current are strong. Again, there is also a clear positive density anomaly on the western boundary in Fig. 5(e).

The anomalous meridional transport can be related to zonal density gradients through the thermal wind relation (Hirschi and Marotzke 2007), thus:

$$f \frac{\partial v}{\partial z} = -\frac{g}{\rho_0} \frac{\partial \rho}{\partial x} \quad \Rightarrow \quad \bar{v}^x(z') = \int_{x_W}^{x_E} v dx = \frac{g}{\rho_0 f} \int_{-H}^{z'} [\rho(WB) - \rho(EB)] dz. \quad (1)$$

where  $\rho_0$  is the mean density,  $f$  is the Coriolis parameter,  $g$  is the acceleration due to gravity and  $\rho(WB)$  and  $\rho(EB)$  are the density anomalies on the western and eastern boundaries. On

218 integrating vertically we obtain an anomalous overturning streamfunction of

$$\psi_{\rho}(z) \approx - \int_{-H}^z \left[ \bar{v}^x(z') - \frac{1}{H} \int_{-H}^0 \bar{v}^x dz \right] dz', \quad (2)$$

219 where the vertical average of  $\bar{v}^x$  has been subtracted out to ensure that  $\psi_{\rho}(z = 0) = \psi_{\rho}(z =$   
 220  $-H) = 0$ .

221 In Fig. 6 we compare the MOC variability  $\text{MOC}(HI) - \text{MOC}(LO)$  (solid lines) with the  
 222 anomalous transport computed from the density anomalies on the western boundary  $\psi_{\rho}(WB)$   
 223 (dashed lines) in the two models. The contribution of density anomalies on the eastern bound-  
 224 ary  $\psi_{\rho}(EB)$  is negligible in CCSM3 and is much smaller than  $\psi_{\rho}(WB)$  in CM2.1 (as indicated in  
 225 Fig. 6b). The MOC variability  $\text{MOC}(HI) - \text{MOC}(LO)$  is defined as the average MOC in ‘high’  
 226 years minus the average MOC in ‘low’ years averaged from 40°N to 45°N, while  $\psi_{\rho}(WB)$  is com-  
 227 puted using Eq. (2) applied to the density fields shown in Fig. 5(b) and 5(e). The dashed lines in  
 228 Fig. 5(b) and 5(e) indicate regions over which density was zonally averaged to estimate  $\psi_{\rho}(WB)$ ,  
 229 that is from the shelf out to the dashed line.

230 The close match between  $\text{MOC}(HI) - \text{MOC}(LO)$  and  $\psi_{\rho}(WB)$  in both models is perhaps not  
 231 unexpected in view of the thermal wind equation. As noted above, this is also a property of the  
 232 coupled, idealized models studied in Buckley (2011). It highlights the close association between  
 233 density anomalies on the western boundary and MOC variability. Understanding how those density  
 234 anomalies are created, how they arrive at the western boundary and what sets their timescale of  
 235 variability, is key to understanding how the MOC varies.

236 **2e. Role of the Mann Eddy**

237 As shown in Figs. 2-4, MOC variability is associated with upper ocean, temperature-dominated  
238 density anomalies at the western boundary near the Grand Banks. Fig. 7 shows mean currents and  
239 (HI)-(LO) composites at 300 m depth in the two models. The (HI)-(LO) composites of each model  
240 reveal that in association with a strong MOC there is anomalously cyclonic circulation in the boxed  
241 region, and a somewhat enhanced Gulf Stream and Labrador Current. These cyclonic anomalies  
242 are in geostrophic balance with the positive buoyancy anomalies shown in Figs. 3(b) and 4(b). We  
243 believe it is significant that these cyclonic anomalies are at the location of the respective model's  
244 representation of the Mann Eddy. In the ocean, the Mann Eddy is a persistent anticyclone swirling  
245 at the end of the separated Gulf Stream to the southeast of the NAC, located approximately between  
246 38°N–45°N and 40°W–50°W (Mann 1967; Meinen et al. 2000). This is the region where the deep  
247 expression of the southward flowing Labrador Current abuts the northward flowing Gulf Stream.  
248 The variability of the Mann Eddy likely modulates the trajectory of the NAC and the strength of  
249 the MOC. We hypothesize that the cyclonic circulation within the boxed regions of the (HI)-(LO)  
250 composites in Fig. 7(b,d) imply that a weakened Mann Eddy is associated with an enhanced MOC.

251 **2f. Role of Labrador Sea Convection**

252 In CCSM3, there is a clear connection between density anomalies that propagate around the sub-  
253 polar gyre, precondition convection, and result in density anomalies that later appear in the 40°N  
254 to 45°N latitude band (see Fig. 5b). Fig. 8(a) shows (HI)-(LO) composite maps of March mixed  
255 layer depth (MLD). The first EOF of MLD variability shown in Fig. 8(b) is very similar to the  
256 (HI)-(LO) composite maps. Cross-correlations of  $T$ ,  $S$ ,  $\rho$  (at 150m depth in the box in the region

257 of maximum MLD variability) against MLD (in the same box) and the MOC index defined in  
258 Fig. 1 are shown in Fig. 8(c,d). Density anomalies are in phase with the MLD anomalies and so it  
259 seems clear that the propagation of density around the subpolar gyre is preconditioning Labrador  
260 Sea deep convection — see the review in (Marshall and Schott 1999). Fig. 8(d) shows that density  
261 anomalies in the Labrador Sea region lead MOC anomalies (see also Danabasoglu 2008). The  
262 propagation of deep density anomalies from the Labrador Sea to the region of maximum MOC  
263 can be seen coming from north of  $50^\circ$  in Fig. 5(c). However, a significant fraction of the density  
264 anomaly at  $42^\circ\text{N}$  does not originate in the Labrador Sea.

265 In CM2.1, the connection between MOC variability and deep convection in the Labrador Sea  
266 is less clear. The principle component time series of EOF1 of MLD does covary with MOC in-  
267 dex however its spatial pattern is a large dipole covering the Labrador Sea region (not shown).  
268 Consequently, cross-correlations between  $(T, S, \rho)$  in the Labrador Sea (northernmost boxed re-  
269 gion shown in Fig. 8) and the maximum MOC (*i.e.*, the index defined in Fig. 1) are insignificant.  
270 Similarly, cross-correlations between  $(T, S, \text{ and } \rho)$  and MLD are not significant since the north-  
271 ern box overlaps the EOF-1 dipole. Fig. 5(f) also indicates that MOC variability is mainly due to  
272 near-surface density anomalies south of  $50^\circ\text{N}$ , with little indication of a role for convection north  
273 of  $50^\circ\text{N}$ .

274 In summary, Labrador Sea convection does seem to play some role in creating density anoma-  
275 lies off George's Bank in CCSM3, but there is little evidence that it is creating density anomalies  
276 there in CM2.1. In both models density anomalies off George's Bank set the strength of the MOC  
277 through thermal wind, and are controlled by the advection of density anomalies around the subpo-  
278 lar gyre.

### 279 **3. Idealized ‘toy model’ of MOC variability**

#### 280 **3a. Construction of an ‘oscillator model’**

281 In the previous section we showed that MOC variability covaries with temperature-dominated  
 282 density anomalies on the western boundary of the subpolar gyre. The dominant timescale of the  
 283 variability appears to depend on the time it takes for the density anomalies to propagate around  
 284 the subpolar gyre and reach the western boundary. We hypothesize, as do Kwon and Frankignoul  
 285 (2011) and Danabasoglu (2008), that such anomalies could be energized by stochastic atmospheric  
 286 forcing. In this section we apply the ideas of Marshall et al. (2001) to formulate a delayed oscillator  
 287 ‘toy model’ of the MOC variability. This is a modification of the canonical model of the interaction  
 288 of ocean with the atmosphere due to Frankignoul and Hasselmann (1977, in the following FH77):

$$\frac{\partial T}{\partial t} = \mathcal{F} - \lambda T, \quad (3)$$

289 where  $T$  denotes a near-surface temperature (FH77 assumed it to be SST),  $\lambda$  is a damping timescale  
 290 (of order of a season) and  $\mathcal{F}$  is the surface forcing (Ekman pumping and turbulent heat flux)  
 291 associated with atmospheric variability. In FH77  $\mathcal{F}$  is taken to be a white noise process, so that  
 292 Eq. (3) predicts a red spectrum for  $T$  on timescales shorter than  $\lambda^{-1}$ , and a flattening on longer  
 293 timescales. This is obviously not a good model of the processes that lead to the spectra shown  
 294 in Fig. 2. which exhibit a pronounced spectral peak at (see below) roughly the time it takes a  
 295 baroclinic Rossby wave to propagate across the basin.

296 We therefore make use of a simple elaboration of Eq. (3) which is capable of capturing a spec-  
 297 tral peak through a delayed oceanic response of  $T$  to external meteorological forcing. Accordingly  
 298 we modify Eq. (3) with a delay term,  $D$ , thus, to represent ocean circulation:

$$\frac{\partial T}{\partial t} = -\tau - \lambda T - DT(t - t_d), \quad (4)$$

299 where

$$\tau = \alpha \mathcal{N} - fT. \quad (5)$$

300 In our interpretation of Eq. (4),  $T$  denotes the strength of upper ocean thermal anomalies on the  
 301 western boundary (for example in the box in Fig. 7),  $\tau$  is the amplitude of the wind stress variability  
 302 (in temperature units) blowing over the basin which is assumed to be decomposed into a stochastic  
 303 component  $\mathcal{N}$  and, possibly, an SST—induced feedback component ( $fT$ ). Key model parameters  
 304 are (they are discussed in much more detail in Marshall et al. 2001):

- 305 •  $\alpha$ : scaling of stochastic wind stress  $\mathcal{N}$  into a temperature tendency,
- 306 •  $\lambda$ : damping due to air-sea interaction,
- 307 •  $f$ : feedback of  $T$  on the wind stress pattern,
- 308 •  $D$  and  $t_d$  measure the strength and time-delay of the feedback of ocean circulation on  $T$ .

309 We present the delay term in Eq. (4) as a representation of advective and wave ocean processes  
 310 that, on long timescales, play a role in setting  $T$ . Clearly it is a highly symbolic characterization of  
 311 the processes at work in the ocean and ocean models. However, it should be noted that, as shown in  
 312 Marshall et al. (2001), a term of this form arises from a consideration of time-dependent Sverdrup  
 313 dynamics and thermohaline circulation dynamics. Here we are agnostic as to the detailed processes  
 314 that control  $D$  and  $t_d$  and, instead, adjust these model parameters to best fit model spectra.

315 For  $f = 0$ , the solution to Eq. (4) in the Fourier domain is given by

$$\hat{T} = -\frac{\alpha \hat{\mathcal{N}}}{i\omega + De^{-i\omega t_d} + \lambda}, \quad (6)$$



316 where  $|\hat{\mathcal{N}}|^2 = 1$ , and  $T(t) = \int \hat{T}(\omega)e^{i\omega t}d\omega$ . Fig. 9 shows the (a) spectra and (b) “free solutions”  
 317 for  $D = 0, 0.1, 0.2$  and  $0.3 \text{ years}^{-1}$  with  $\alpha = 1 \text{ K}\cdot\text{m}^2\cdot\text{N}^{-1}$ ,  $t_d = 8 \text{ years}$ , and  $\lambda = 2\pi/32 \text{ years}^{-1}$ ,  
 318 as in Plate 1 of Czaja and Marshall (2000). The free (or unforced) solutions, are obtained by setting  
 319  $\alpha = 0$ , initializing with a cosine function for  $t < 0$ , and then allowing them to decay away in time,  
 320 thus:

$$T_{\text{free}} \propto e^{-\gamma t/2} \cos(\omega_0 t), \quad (7)$$

321 where  $\omega_0$  measures the frequency of the oscillation and  $\gamma$  the decay rate. The parameter  $\gamma$  in Eq. (7)  
 322 is obtained by a least squares fit over the first few oscillations of the free solutions. Decay rates  
 323 in Fig. 9 are  $\gamma = 2\pi/16, 2\pi/13.5, 2\pi/29.5$ , and  $2\pi/132.5 \text{ (years)}^{-1}$  for  $D = 0, 0.1, 0.2$  and  $0.3$   
 324  $\text{(years)}^{-1}$  respectively. From these decay rates and  $\omega_0$  we can define a Q-factor:

$$q = \frac{\omega_0}{\gamma}. \quad (8)$$

325 The Q-factor measures the number of distinct oscillations and is approximately 0, 1, 2.5 and 11.5  
 326 in the four cases. The Q-factor can also be measured directly from the spectral density of  $T$  as the  
 327 peak frequency divided by the bandwidth of the range of frequencies for which the energy is half  
 328 its peak value.

### 329 **3b.** *Fitting the oscillator model to the ‘observed’ spectra*

330 To fit the delayed oscillator model to observed spectra it is useful to consider two extreme fre-  
 331 quency limits implied by Eq. (6) as follows:

$$\lim_{\omega \rightarrow 0} |\hat{T}|^2 = \left( \frac{\alpha}{D + \lambda} \right)^2 \quad (9)$$

332 and

$$\lim_{\omega \rightarrow \infty} |\hat{T}|^2 = \frac{\alpha^2}{\omega^2}. \quad (10)$$

333 We first solve for  $\alpha$  in the  $\omega \rightarrow \infty$  limit, then solve for  $D + \lambda$  using the  $\omega \rightarrow 0$  limit. Note that the  
 334 time delay  $t_d$  is tightly constrained by the frequency of the spectral peak because resonance occurs  
 335 when  $\omega t_d = \pi/2$ , giving an oscillation period of  $4t_d$  in the absence of damping (*i.e.*,  $\lambda = 0$ ). Also  
 336 note that  $D$  determines the height of the spectral peak, and  $\lambda$  acts as a limiter on growth towards  
 337 low frequencies.

338 Figs. 10(a,b) show normalized spectra (blue curves) for CCSM3 and CM2.1 and the recon-  
 339 structed spectra using a purely statistical AR<sub>15</sub> least squares fit (black curves) and the delayed  
 340 oscillator model in Eq. (4) (red curves) fitted manually using the statistical fit as a guide<sup>2</sup>. The  
 341 fitted delayed oscillator parameters in CCSM3 are

- 342 •  $\alpha = 0.6$ ,  $t_d = 7$  years,  $D = 0.17$  years<sup>-1</sup> and  $\lambda = 0.157$  years<sup>-1</sup>,

343 while in CM2.1 they are

- 344 •  $\alpha = 0.4$ ,  $t_d = 5$  years,  $D = 0.2$  years<sup>-1</sup> and  $\lambda = 0.063$  years<sup>-1</sup>.

345 From these parameters we can deduce  $\omega_0$  and  $\gamma$  in Eq. (7) and then compute the Q-factor in  
 346 CCSM3:

- 347 •  $\omega_0 = 2\pi/24$  years<sup>-1</sup>,  $\gamma = 2\pi/43$  years<sup>-1</sup>  $\Rightarrow q = 1.8$

348 and for CM2.1:

---

<sup>2</sup>Our delayed oscillator model has only three free parameters, yet it is compared to a higher-order autoregressive model here

349 •  $\omega_0 = 2\pi/21.5 \text{ years}^{-1}$ ,  $\gamma = 2\pi/38 \text{ years}^{-1} \Rightarrow q = 1.76$ .

350 We note in passing that these fitted delay times  $t_d$  are broadly consistent with the transit time  
 351 of Rossby waves in the North Atlantic at 40°N. Using data from Tulloch et al. (2009), we estimate  
 352 the observed Rossby wave phase speed in the eastern Atlantic to be about  $2 \text{ cm}\cdot\text{s}^{-1}$  from 40°N to  
 353 50°N, which gives transit times of the order of 5 to 10 years. Also, as pointed out by Kwon and  
 354 Frankignoul (2011), the regime from years 51-350 in CCSM are more predictable than all of the  
 355 years. We estimate the Q-factor for this range of years to be about  $q = 3$ .

### 356 **3c. Implications for predictability**

357 The delayed oscillator models fit the spectral peak, some of the higher harmonics, and the low  
 358 frequencies quite well, indicating that they can perhaps be used to make predictions. Here we  
 359 show a sample prediction from such a fitted toy model and compare it with a purely statistical  
 360 prediction, assuming perfect initial conditions. We simply train our toy model on the MOC time  
 361 series, but bear in mind that a real prediction would require training our model against a subsurface  
 362 temperature fingerprint, as done in Mahajan et al. (2011b).

363 Figs. 10(c,d) show ensemble mean predictions in CCSM3 and CM2.1 with the model param-  
 364 eters given above. To create the predictions, ensembles for the statistical and delayed oscillator  
 365 models were initialized with the MOC from the 15 years preceding the starting year, which is  
 366 denoted in the figure by vertical dashed lines. As time progresses, the ensemble means decay  
 367 away because the ensemble members become uncorrelated. The predictions shown here are the  
 368 ensemble means scaled by those decay rates ensuring that the magnitudes of the predictions re-  
 369 main roughly constant in time. Both the statistical ( $\text{AR}_{15}$ ) and delayed oscillator predictions track

370 the MOC for a couple of oscillations before losing the phase, consistent with Q-factors of about 2.  
371 As expected from their power spectra, the statistical and delayed oscillator predictions are almost  
372 identical for the first couple of cycles, and then diverge as either fast timescale errors accumulate  
373 or long timescale errors start to appear. However the quality of the predictions depend on how rep-  
374 resentative the predicted years are to the average behavior over the 500 year time series. Note that  
375 the predictions shown in Fig. 10 correspond to instances where the prediction tracks MOC longer  
376 than suggested by the model’s Q-factors. Other initial conditions result in predictions which lose  
377 the phase of the MOC within a few years.

378 Our results are broadly in accord with those of Mahajan et al. (2011b), who attempted to pre-  
379 dict AMOC variations using an autoregressive model (AR2) tuned to the subsurface temperature  
380 anomalies, or “AMOC fingerprints”, defined in Zhang (2008). They predicted a drop in AMOC  
381 strength in the few years following its peak in 2005. This was based on the fidelity of their AR2  
382 model in hindcasts of observed subsurface temperature anomalies and the close connection be-  
383 tween AMOC variability and subsurface temperature variability in CM2.1. Mahajan et al. (2011b)  
384 also found that hindcasts from their AR2 model show comparable skill whether they are trained  
385 on 500 years or only 50 years of CM2.1 data, although they note that the 20 year spectral peak  
386 in CM2.1 is not robust across models or the observations. Msadek et al. (2010) also argued that  
387 AMOC in CM2.1 is predictable for up to 20 years.

## 388 **4. Summary and Discussion**

389 By using the same diagnostic tools to study variability in two coupled climate models, we have  
390 identified aspects that are common to them both. In particular we find that:

391 (i) AMOC variability is associated with upper ocean (top 500 m to 1 km) density anomalies on  
392 the western margin of the basin in the region of the Mann Eddy. These anomalies modulate the  
393 trajectory and strength of the North Atlantic Current. The importance of the western margin is a  
394 direct consequence of the thermal wind relation and is independent of the mechanism that creates  
395 those density anomalies.

396 (ii) Density anomalies in this key region are part of a larger-scale density pattern that propagates  
397 around the subpolar gyre. These act as a ‘pacemaker’ of AMOC variability.

398 (iii) Density anomalies are dominated by temperature, with salinity playing a lesser role.

399 (iv) The timescale of AMOC variability is broadly consistent with the inherent timescale set by  
400 the transit time of first baroclinic mode Rossby waves at 45°N.

401 (v) Although we are unable to identify how the density anomalies are created, they appear  
402 to emanate along the zero-wind-stress curl line separating the subtropical and subpolar gyres. It  
403 is here that modeled (NAO) wind variability is a maximum. We suspect that this external wind  
404 forcing gives rise to thermocline undulations as in Frankignoul et al. (1997) which, when they strike  
405 the western boundary, spin up the AMOC. A hierarchy of ocean-only and coupled experiments  
406 would be required to confirm or reject this conjecture.

407 (vi) Density anomalies entering regions of deep convection (e.g. the Labrador Sea) can act to  
408 precondition convection. This is clearly evident in CCSM3 but less important in CM2.1. Deep,  
409 convectively-formed anomalies can then propagate southward on the western boundary current to  
410 the region of the Mann Eddy and thence induce changes in the AMOC.

411 (v) Fitting a delayed oscillator model to the spectra found in the two models suggests that  
412 AMOC variability has a Q-factor of around 2, implying predictability out to a couple of cycles or  
413 so. This can be used as a minimalist model against which more complex predictability systems

414 can be compared.

415 Finally, it should be noted that an association between MOC variability and density anomalies  
416 on the western margin of the gyre (off-shore of the Grand Banks in the region of the Mann Eddy)  
417 is, in retrospect, not surprising. Zonal and vertical integration of the thermal wind equation links  
418 changes in geostrophic contributions to MOC to those of depth integrated buoyancy differences  
419 between the zonal endpoints. To the extent that anomalies on the eastern boundary are much  
420 smaller than anomalies on the west, anomalies on the west become the dominant contributor to  
421 MOC variability on decadal timescales. This could explain why, for example, MOC variability  
422 is so sensitive to model formulation, both between models and in the same model when changes  
423 are made to its resolution, overflow parameterizations etc. For example Danabasoglu et al. (2011)  
424 and Yeager and Danabasoglu (2011) describe AMOC variability in CCSM4 and find significant  
425 sensitivity to how Nordic Sea overflows are parameterized. The dynamics of the ocean in the  
426 region of the Mann eddy is a ‘cross roads’ where potential vorticity anomalies created in distant  
427 parts of the basin are brought together and interact. This is indeed a very complex region and will  
428 be sensitive to model resolution and parameterization.

## 429 **5. Acknowledgements**

430 This study is part of a collaborative project between MIT, GFDL and NCAR supported from Jim  
431 Todd’s NOAA Clivar program. Ross Tulloch is supported as a NOAA postdoctoral fellow. We  
432 thank David Ferreira and Martha Buckley for helpful discussions. Thanks also to Tom Delworth  
433 (GFDL) and Gokhan Danabasoglu (NCAR) for making available their model results and their  
434 openness in discussing them.

435

436

## APPENDIX A

437

438

### Climate models

439 The NCAR CCSM3 coupled model is described in detail in Danabasoglu (2008). It uses the  
440 Community Atmosphere Model 3 (CAM3), the Community Land Model Version 3 (CLM3), the  
441 Parallel Ocean Program version 1.4 (POP1.4) and the Community Sea Ice Model (CSIM). The  
442 atmospheric model is at T85 resolution with 26 vertical levels, and the ocean model has nominal  
443  $1^\circ$  horizontal resolution and 40 vertical levels. Here we analyze years 101-600 of the 700 year  
444 present day (1990) control integration experiment b30.009.

445 The GFDL 2.1 coupled model, described in Delworth et al. (2006), has  $2.5^\circ \times 2^\circ$  horizontal  
446 resolution and 24 vertical levels in the atmosphere, and uses the Modular Ocean Model 4 (MOM4),  
447 which has nominal  $1^\circ$  horizontal resolution and 50 vertical levels. Here we analyze years 1-500 of  
448 the pre-industrial (1860) control experiment 1860-D4.

## References

- 449 **References**
- 450 Bretherton, C. S., M. Widmann, V. P. Dymnikov, J. M. Wallace, and I. Blade, 1999: The effective  
451 number of spatial degrees of freedom of a time-varying field. *J. Climate*, **12**, 1990–2009.
- 452 Buckley, M. W., 2011: Mechanisms of meridional overturning circulation variability in idealized  
453 coupled models. *J. Climate*, Submitted.
- 454 Colin de Verdière, A. and T. Huck, 1999: Baroclinic instability: an oceanic wavemaker for inter-  
455 decadal variability. *J. Phys. Oceanogr.*, **29**, 893–910.
- 456 Czaja, A. and J. C. Marshall, 2000: On the interpretation of AGCMs response to prescribed time-  
457 varying SST anomalies. *Geophys. Res. Lett.*, **27**, 1927–1930.
- 458 — 2001: Observations of atmosphere-ocean coupling in the North Atlantic. *Quart. J. Roy. Meteor.*  
459 *Soc.*, **127**, 1893–1916.
- 460 Dai, A., A. Hu, G. A. Meehl, W. M. Washington, and W. G. Strand, 2005: Atlantic thermohaline  
461 circulation in a coupled general circulation model: unforced variations versus forced changes.  
462 *J. Climate*, **18**, 3270–3293.
- 463 Danabasoglu, G., 2008: On multidecadal variability of the meridional overturning circulation in  
464 the Community Climate System Model Version 3. *J. Climate*, **21**, 5524–5544.
- 465 Danabasoglu, G., S. G. Yeager, Y.-O. Kwon, J. J. Tribbia, A. Phillips, and J. Hurrell, 2011: Vari-  
466 ability of the Atlantic Meridional Overturning Circulation in CCSM4. *J. Climate*, Submitted.
- 467 Delworth, T. and R. J. Greatbatch, 2000: Multidecadal thermohaline circulation variability driven  
468 by atmospheric surface flux forcing. *J. Climate*, **13**, 1481–1495.



- 469 Delworth, T., S. Manabe, and R. J. Stouffer, 1993: Interdecadal variations of the thermohaline  
470 circulation in a coupled ocean-atmosphere model. *J. Climate*, **6**, 1993–2011.
- 471 — 1997: Multidecadal climate variability in the Greenland Sea and surrounding regions: a coupled  
472 model simulation. *Geophys. Res. Lett.*, **24**, 257–260.
- 473 Delworth, T. and M. E. Mann, 2000: Observed and simulated multidecadal variability in the North-  
474 ern Hemisphere. *Clim. Dyn.*, **16**, 661–676.
- 475 Delworth, T. L., A. J. Broccoli, A. Rosati, R. J. Stouffer, V. Balaji, J. A. Beesley, W. F. Cooke, K. W.  
476 Dixon, J. Dunne, K. A. Dunne, J. W. Durachta, K. L. Findell, P. Ginoux, A. Gnanadesikan, C. T.  
477 Gordon, S. M. Griffies, R. Gudgel, M. J. Harrison, I. M. Held, R. S. Hemler, L. W. Horowitz,  
478 S. A. Klein, T. R. Knutson, P. J. Kushner, A. R. Langenhorst, H.-C. Lee, S.-J. Lin, J. Lu, S. L.  
479 Malyshev, P. C. D. Milly, V. Ramaswamy, J. Russell, M. D. Schwarzkopf, E. Shevliakova, J. J.  
480 Sirutis, M. J. Spelman, W. F. Stern, M. Winton, A. T. Wittenberg, B. Wyman, F. Zeng, , and  
481 R. Zhang, 2006: GFDL’s CM2 global coupled climate models. Part I: formulation and simulation  
482 characteristics. *J. Climate*, **19**, 643–674.
- 483 Dong, B. and R. T. Sutton, 2005: Mechanism of interdecadal thermohaline circulation variability  
484 in a coupled ocean-atmosphere GCM. *J. Climate*, **18**, 1117–1135.
- 485 Eden, C. and J. Willebrand, 2001: Mechanism of interannual to decadal variability of the North  
486 Atlantic Circulation. *J. Climate*, **14**, 2266–2280.
- 487 Frankcombe, L. M., H. A. Dijkstra, and A. v. Heydt, 2009: Coherent multidecadal variability in  
488 north atlantic sea level. *Geophys. Res. Lett.*, **36**, doi:10.1029/2009GL039455.

- 489 Frankignoul, C. and K. Hasselmann, 1977: Stochastic climate models, part ii application to sea-  
490 surface temperature anomalies and thermocline variability. *Tellus*, **29**, 289–305.
- 491 Frankignoul, C. and P. Müller, 1979: Quasi-geostrophic response of an infinite beta-plane ocean  
492 to stochastic forcing by the atmosphere. *J. Phys. Oceanogr.*, **9**, 104–127.
- 493 Frankignoul, C., P. Müller, and E. Zurita, 1997: A simple model of the decadal response of the  
494 ocean to stochastic wind forcing. *J. Phys. Oceanogr.*, **27**, 1533–1546.
- 495 Griffies, S. M. and E. Tziperman, 1995: A linear thermohaline oscillator driven by stochastic  
496 atmospheric forcing. *J. Climate*, **8**, 2440–2453.
- 497 Hawkins, E. and R. Sutton, 2009: Decadal predictability of the atlantic ocean in a coupled gcm:  
498 Forecast skill and optimal perturbations using linear inverse modeling. *J. Climate*, **22**, 3960–  
499 3978.
- 500 Hirschi, J. and J. Marotzke, 2007: Reconstructing the meridional overturning circulation from  
501 boundary densities and the zonal wind stress. *J. Phys. Oceanogr.*, **37**, 743–763.
- 502 Hurrell, J. W., M. Visbeck, A. J. Busalacchi, R. A. Clarke, T. L. Delworth, R. R. Dickson, W. E.  
503 Johns, K. P. Koltermann, Y. Kushnir, D. Marshall, C. Muaritzen, M. S. McCartney, A. Piola,  
504 C. Reason, G. Reverdin, F. Schott, R. Sutton, I. Wainer, and D. Wright, 2006: Atlantic climate  
505 variability and predictability: A CLIVAR perspective. *J. Climate*, **19**, 5100–5121.
- 506 Jayne, S. R. and J. Marotzke, 2001: The dynamics of ocean heat transport variability. *Rev. Geo-*  
507 *phys.*, **3**, 384–411.
- 508 Johns, W. E., M. O. Baringer, L. M. Beal, S. A. Cunningham, T. Kanzow, H. L. Bryden, J. J. M.

- 509 Hirschi, J. Marotzke, C. S. Meinen, B. Shaw, and R. Curry, 2011: Continuous, array-based  
510 estimates of Atlantic ocean heat transport at 26.5°n. *J. Climate*, **24**, 2429–2449.
- 511 Jungclaus, J. H., H. Haak, M. Latif, and U. Mikolajewicz, 2005: Arctic-North Atlantic interactions  
512 and multidecadal variability of the meridional overturning circulation. *J. Climate*, **18**, 4013–  
513 4031.
- 514 Kushnir, Y., 1994: Interdecadal variations in North Atlantic sea surface temperature and associated  
515 atmospheric condition. *J. Climate*, **7**, 141–157.
- 516 Kwon, Y.-O. and C. Frankignoul, 2011: Stochastically-driven multidecadal variability of the At-  
517 lantic meridional overturning circulation in CCSM3. *Clim. Dyn.*, doi:10.1007/s00382-011-1040-  
518 2.
- 519 Leetmaa, A. and J. Marshall, 2006: Workshop report: Atlantic Decadal  
520 Predictability and Plan for Next Steps. Technical report, U.S. Atlantic  
521 Meridional Overturning Circulation Science Team, available online at  
522 [http://www.atlanticmoc.org/pubs/Atlantic\\_Predictability\\_0606.pdf](http://www.atlanticmoc.org/pubs/Atlantic_Predictability_0606.pdf).
- 523 Mahajan, S., R. Zhang, and T. L. Delworth, 2011a: Impact of the Atlantic Meridional Overturn-  
524 ing Circulation (AMOC) on arctic surface air temperature and sea-ice variability. *J. Climate*,  
525 doi:10.1175/2011JCLI4002.1.
- 526 Mahajan, S., R. Zhang, T. L. Delworth, S. Zhang, A. J. Rosati, and Y.-S. Chang, 2011b: Predicting  
527 Atlantic meridional overturning circulation (AMOC) variations using subsurface and surface  
528 fingerprints. *Deep-Sea Res.*, doi:10.1016/j.dsr2.2010.10.067.

- 529 Mann, C. R., 1967: The termination of the Gulf Stream and the beginning of the North Atlantic  
530 Current. *Deep-Sea Res.*, **14**, 337–359.
- 531 Marshall, J. and F. Schott, 1999: Open-ocean convection: observations, theory and models. *Rev.*  
532 *Geophys.*, **37**, 1–64.
- 533 Marshall, J. C., H. Johnson, and J. Goodman, 2001: A study of the interaction of the north atlantic  
534 oscillation with ocean circulation. *J. Climate*, **14**, 1399–1421.
- 535 Meinen, C. S., D. R. Watts, and R. A. Clarke, 2000: Absolutely referenced geostrophic velocity  
536 and transport on a section across the North Atlantic Current. *Deep-Sea Res.*, **47**, 309–322.
- 537 Msadek, R., K. W. Dixon, T. L. Delworth, and W. Hurlin, 2010: Assessing the predictability of the  
538 Atlantic meridional overturning circulation and associated fingerprints. *Geophys. Res. Lett.*, **37**,  
539 L19608, doi:10.1092/2010GL044517.
- 540 Oka, A. and H. Hasumi, 2006: Effects of model resolution on salt transport through northern high-  
541 latitude passages and atlantic meridional overturning circulation. *Ocean Model*, **13**, 126–147.
- 542 Olsen, S. M., B. Hansen, D. Quadfasel, and S. Osterhus, 2008: Observed and modelled stability of  
543 overflow across the Greenland-Scotland ridge. *Nature*, **455**, 519–522.
- 544 Sévellec, F. and A. V. Fedorov, 2011: Stability of the Atlantic meridional overturning circulation  
545 and stratification in a zonally-averaged ocean model: the effects of freshwater flux, wind stress,  
546 and diapycnal diffusion. *Deep-Sea Res.*, in press, doi:10.1016/j.dsr2.2010.10.070.
- 547 Te Raa, L. A., J. Gerrits, and H. A. Dijkstra, 2004: Identification of the mechanism of interdecadal  
548 variability in the North Atlantic Ocean. *J. Phys. Oceanogr.*, **34**, 2792–2807.

- 549 Tulloch, R. T., J. C. Marshall, and K. S. Smith, 2009: Interpretation of the propagation of surface  
550 altimetric observations in terms of planetary waves and geostrophic turbulence. *J. Geophys. Res.*,  
551 **114**, doi:10.1029/2008JC005055.
- 552 Tziperman, E., L. Zanna, and C. Penland, 2008: Non-normal thermohaline circulation dynamics  
553 in a coupled ocean-atmosphere gcm. *J. Phys. Oceanogr.*, **38**, 588–604.
- 554 Weaver, A. J., J. Marotzke, P. F. Cummins, and E. S. Sarachik, 1993: Stability and variability of  
555 the thermohaline circulation. *J. Phys. Oceanogr.*, **23**, 39–60.
- 556 Weaver, A. J. and Valcke, 1998: On the variability of the thermohaline circulation in the GFDL  
557 coupled model. *J. Climate*, **11**, 759–767.
- 558 Yeager, S. G. and G. Danabasoglu, 2011: Sensitivity of Atlantic Meridional Overturning Circula-  
559 tion variability to parameterized Nordic Sea overflows in CCSM4. *J. Climate*, Submitted.
- 560 Yoshimori, M., C. C. Raible, T. F. Stocker, and M. Renold, 2010: Simulated decadal oscillations of  
561 the Atlantic meridional overturning circulation in a cold climate state. *Clim. Dyn.*, **34**, 101–121,  
562 doi:10.1007/s00382-009-0540-9.
- 563 Zhang, D., R. Msadek, M. J. McPhaden, and T. L. Delworth, 2011: Multidecadal variability of  
564 the North Brazil Current and its connection to the Atlantic meridional overturning circulation. *J.*  
565 *Geophys. Res.*, **116**, C04012, doi:10.1092/2010JC006812.
- 566 Zhang, R., 2008: Coherent surface-subsurface fingerprint of the Atlantic meridional overturning  
567 circulation. *Geophys. Res. Lett.*, **35**, L20705.

568 Zhu, X. and J. Jungclaus, 2008: Interdecadal variability of the meridional overturning circulation  
569 as an ocean internal mode. *Clim. Dyn.*, doi:10.1007/s00382-008-0383-9.

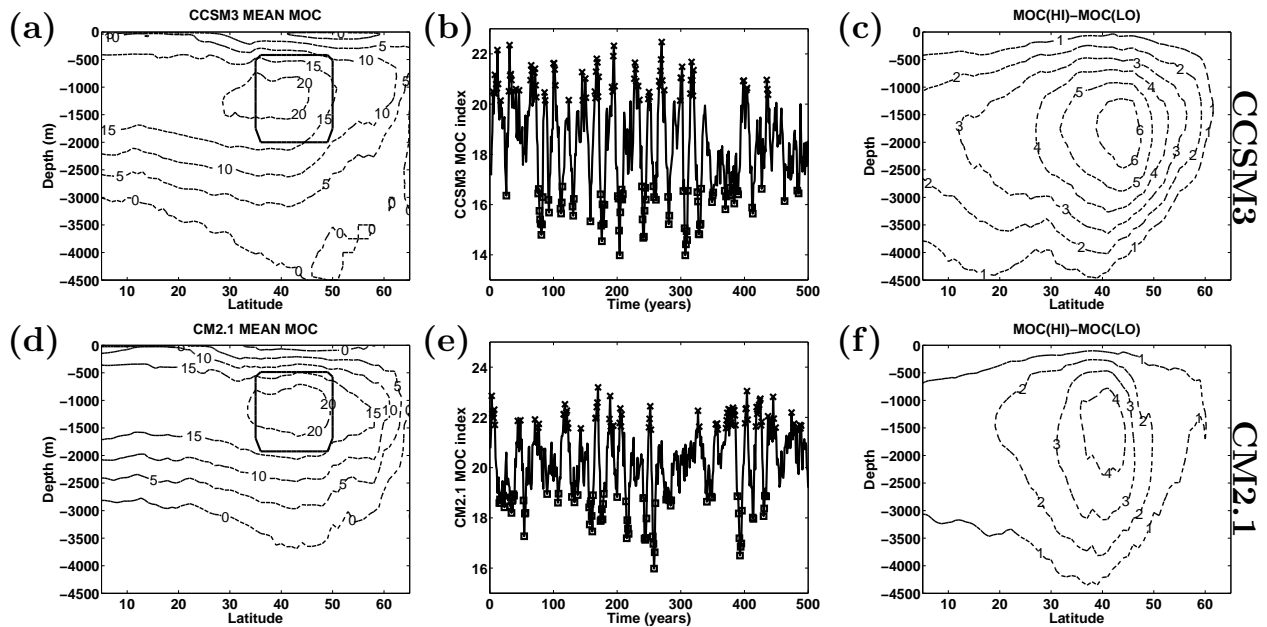


Figure 1: (a) Eulerian-mean MOC (in units of Sv) in the Atlantic in CCSM3 and (b) time series of the MOC index, defined as the average MOC from 35°N to 50°N and 1800 m to 500 m depth, as indicated by the black box in (a). Years marked by x's (squares) denote years that are more than one standard deviation above (below) the time mean. These are used to construct composite maps. (c) The MOC averaged over years marked by x's minus the MOC averaged over years marked by squares, *i.e.*, the MOC(HI)-MOC(LO). The same variables are plotted for CM2.1 in (d), (e) and (f).

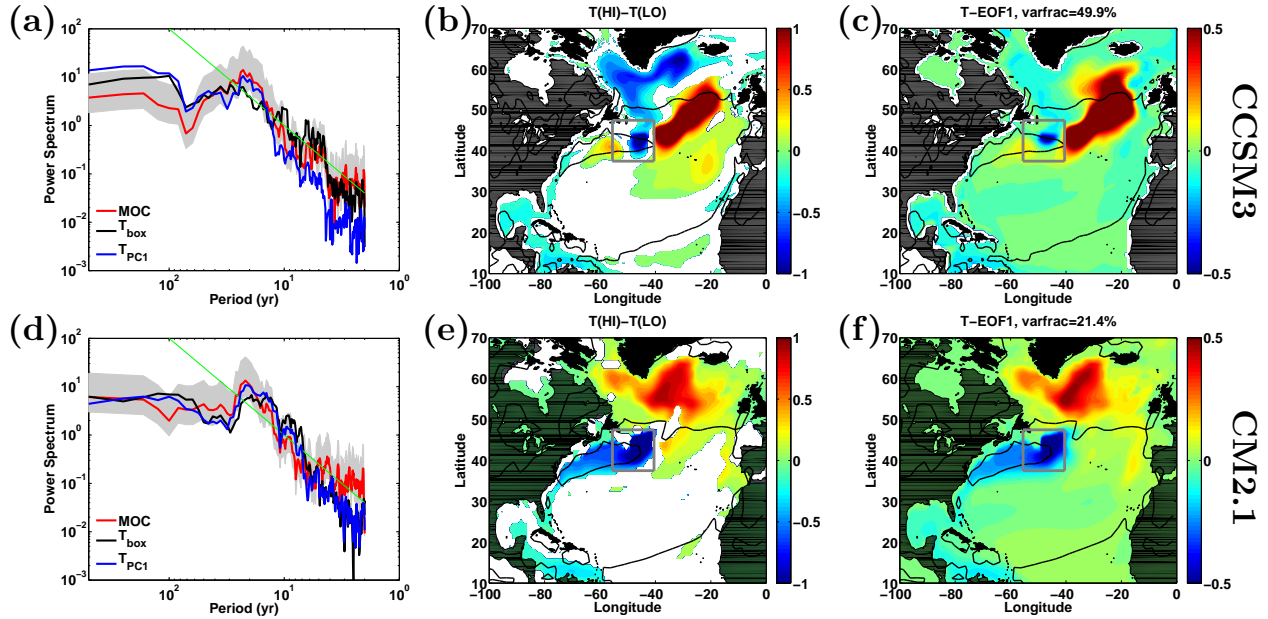


Figure 2: (a) Normalized power spectra of the MOC index (red), temperature (K) averaged over the top 1 km in the gray-boxed regions shown (b) and (c) (black), and the first principal component of temperature (K) in the top 1 km (blue) in CCSM3. The green line indicates a  $-2$  spectral slope and the gray shading is a 95% confidence interval. (b) Composite (HI)-(LO) map of temperature averaged over the top 1 km, obtained by subtracting the low-index composite from the high-index composite, years marked by x's and squares respectively in Fig. 1(b). White shading indicates regions that are not significant at the 95% confidence level. (c) First EOF of temperature averaged over the top 1 km. The black contour indicates the time-mean zero-wind-stress-curl line. The same variables are plotted for CM2.1 in (d), (e), (f), see text for details.



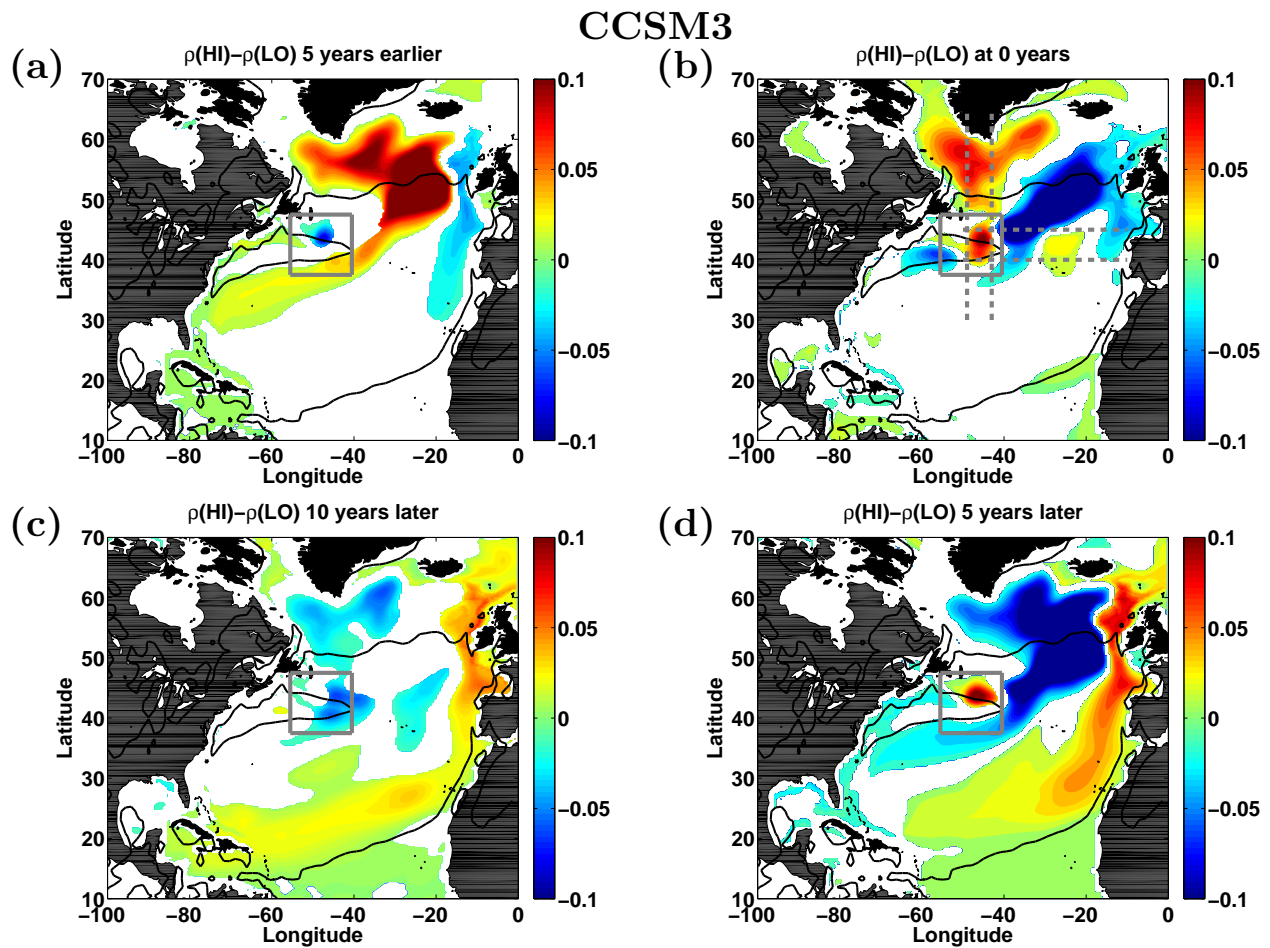


Figure 3: Composite maps of potential density ( $\text{kg}\cdot\text{m}^{-3}$ ) averaged over the top 1 km using the index described in Fig. 2 for CCSM3. (a) The 5-years-earlier map is obtained by subtracting the (low index – 5-years) composite from the (high index – 5-years) composite. (b) As in (a) but at the composite index years, (d) as in (a) but 5 years after the composite years, (c) as in (a) but 10 years after the composite years. Thus, the anomalies evolve in time from the top left to the bottom left. White shading indicates regions that are not significant at the 95% confidence level.

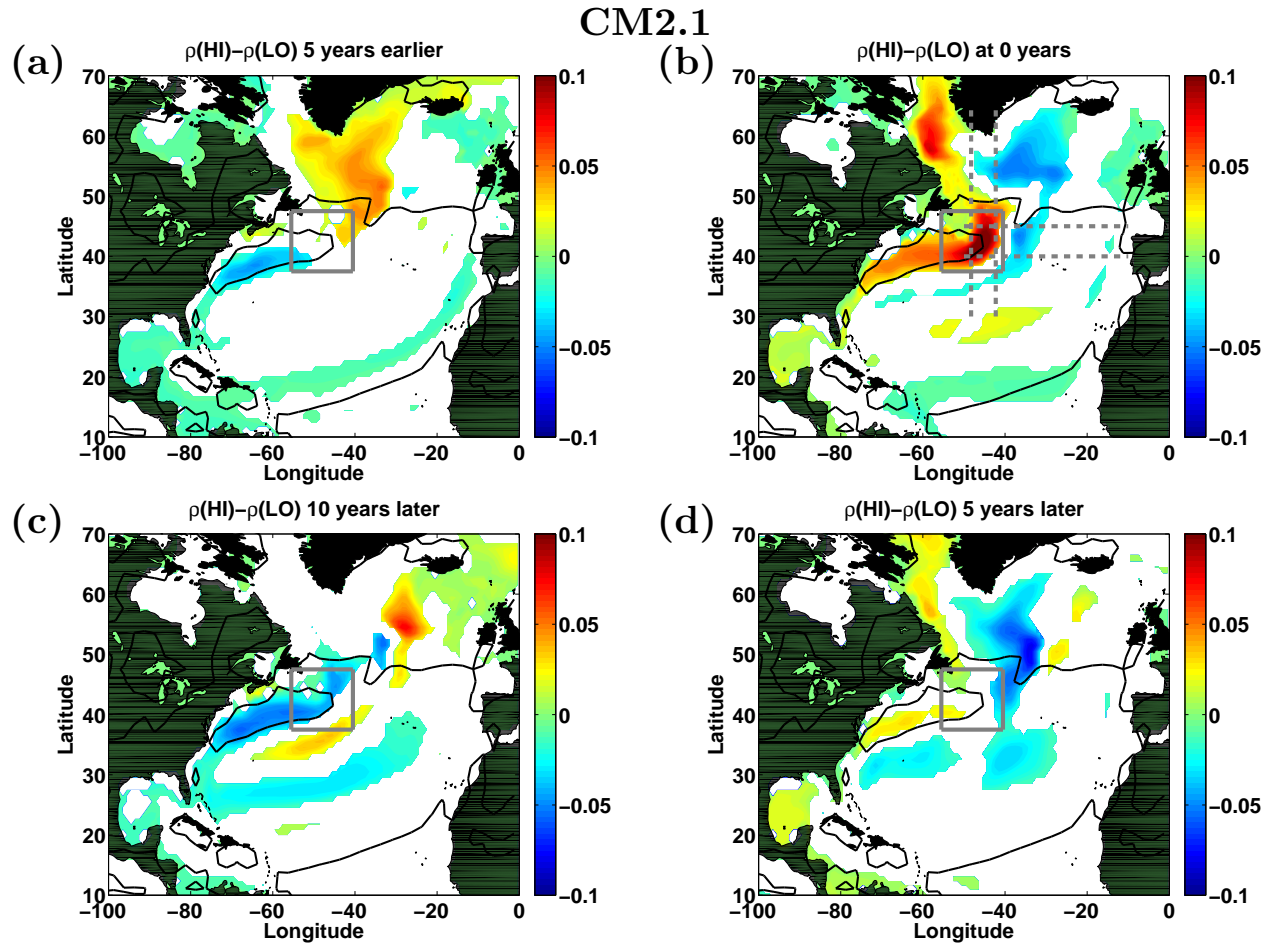


Figure 4: Same as Fig. 3 but for CM2.1.

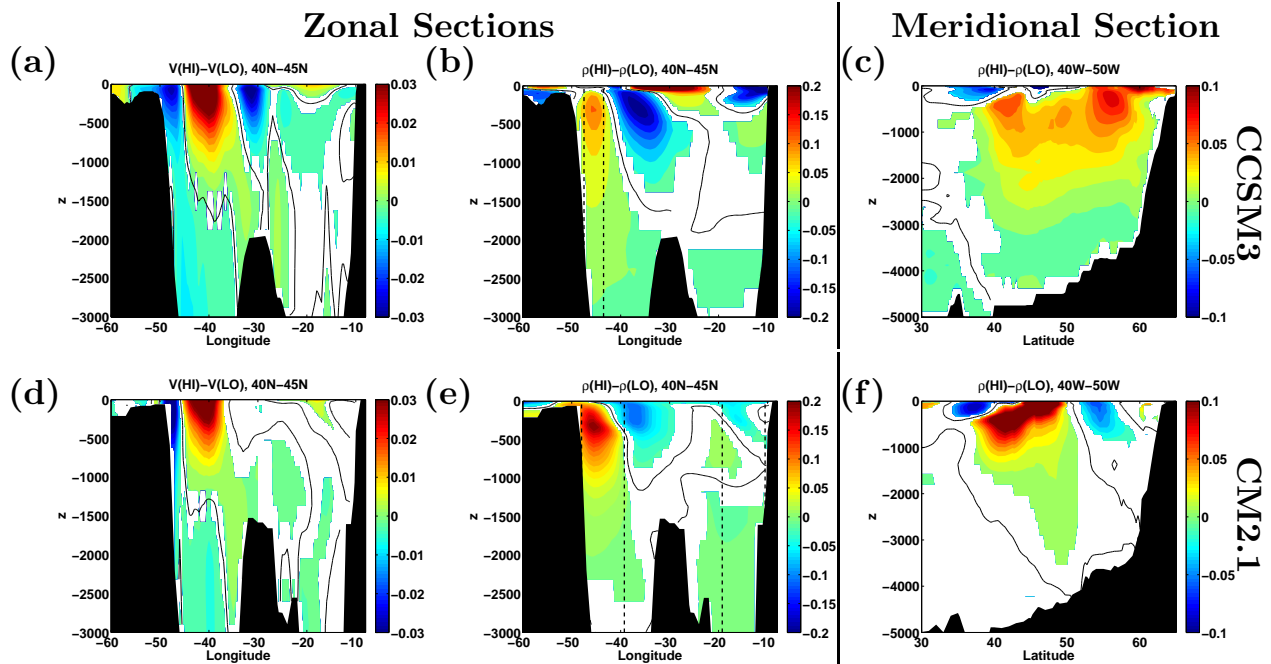


Figure 5: Composite zonal and meridional cross-sections of meridional velocity ( $\text{m}\cdot\text{s}^{-1}$ ) and density ( $\text{kg}\cdot\text{m}^{-3}$ ) in CCSM3 (top row) and CM2.1 (bottom row). The zonal cross-section averaged from  $40^\circ\text{N}$  to  $45^\circ\text{N}$  and the meridional cross-section averaged from  $40^\circ\text{W}$  to  $50^\circ\text{W}$  (land points were excluded from the zonal mean). Dashed lines in (b) and (e) indicate the extent away from the shelf that  $\rho$  was averaged over to compute  $\rho_{WB}$  and  $\rho_{EB}$  (the contribution of  $\rho_{EB}$  in CCSM3 was negligible because  $\int_H^0 \rho dz \approx 0$ ) in Fig. 6. White shading indicates regions that are not significant at the 95% confidence level.

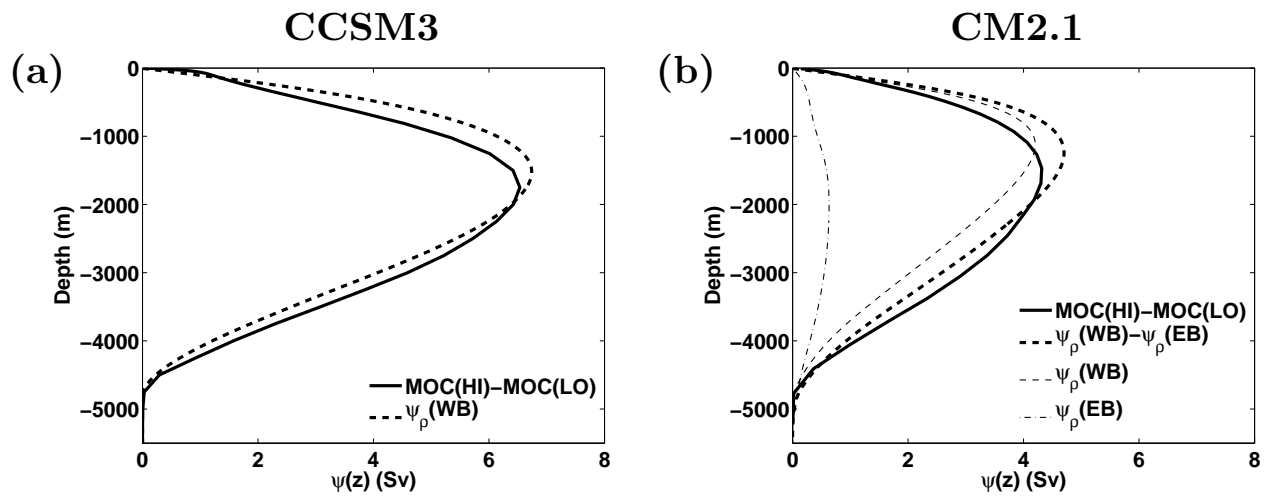


Figure 6: (HI)-(LO) index composite mean MOC averaged from  $40^\circ\text{N}$  to  $45^\circ\text{N}$  (solid lines) and anomalous streamfunction computed from the composite zonal cross-sections of density (dashed lines) in Figs. 5(b) and (e) using Eq. (2). Note that density anomalies on the eastern boundary are negligible in CCSM3. See text for details.

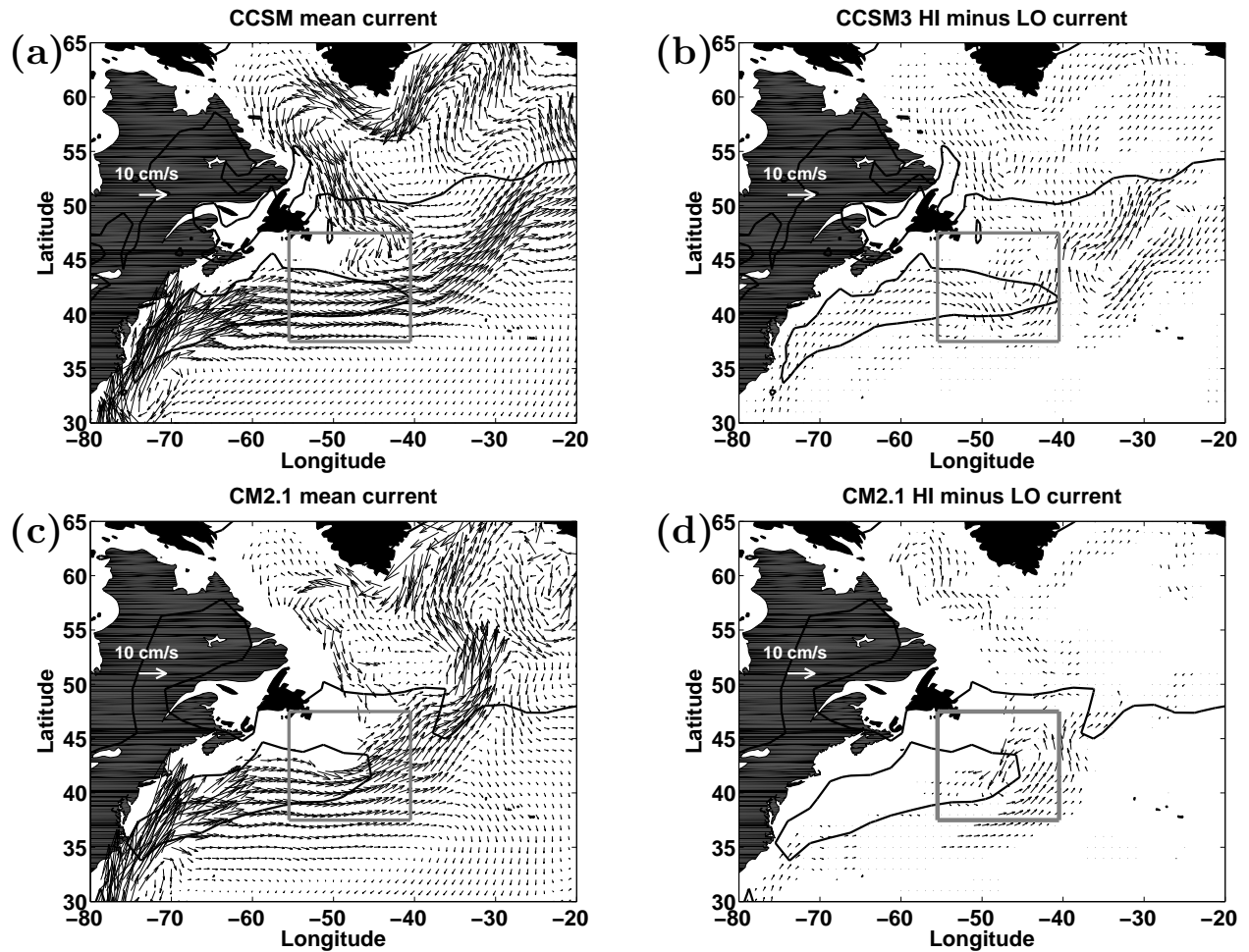


Figure 7: (a) Mean velocity and (b) composite maps of velocity using the index described in Fig. 2 near 300 m (layer 17) in CCSM3. (c) Mean velocity and (d) composites near 300 m (layer 27) in CM2.1. Only vectors significant at the 95% confidence level are shown.

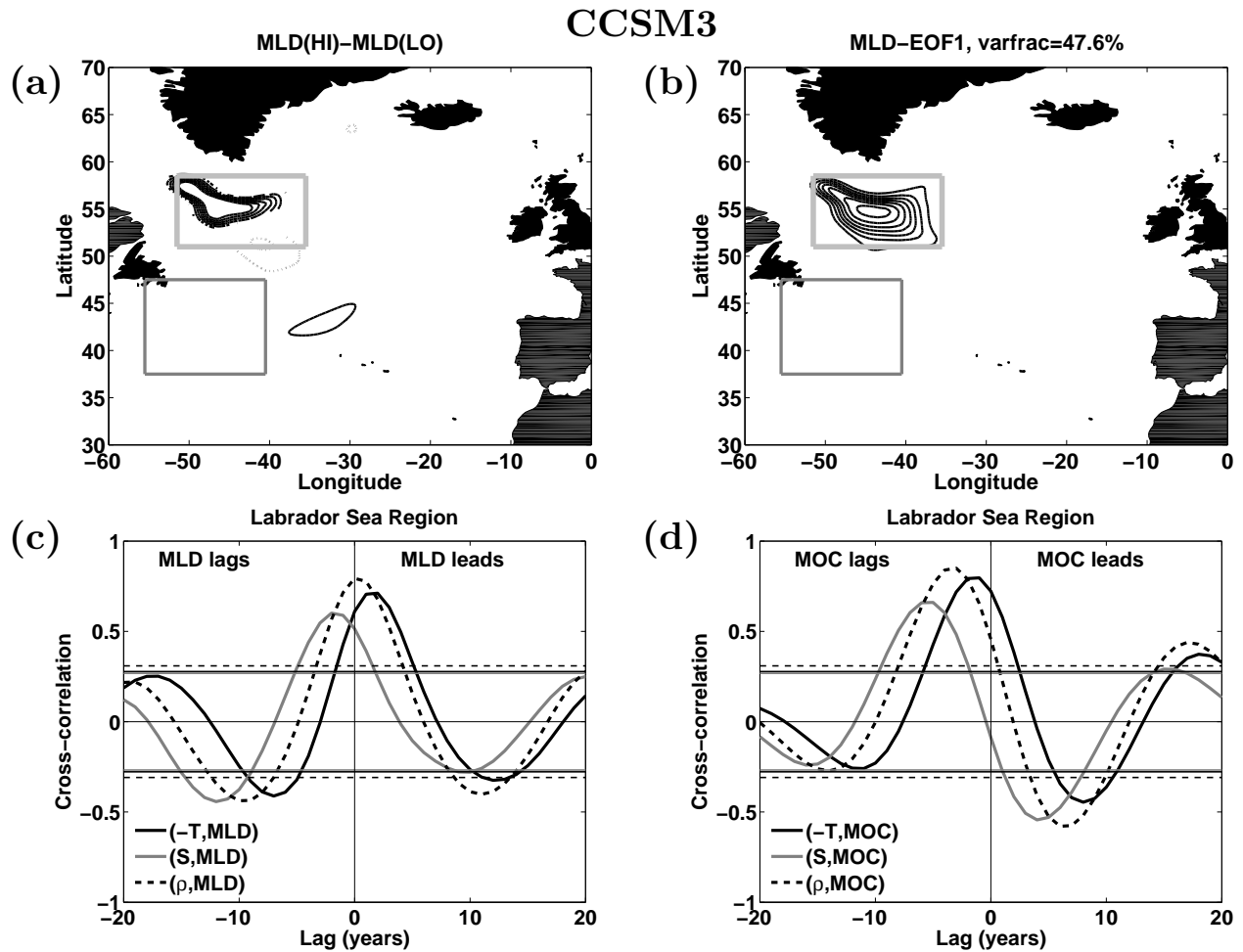


Figure 8: (a) Contours of March mixed layer depth (m) in CCSM3 using the index described in Fig. 2. Thick solid contours are 100 m to 700 m spaced by 100 m, while gray-dotted contours show -100 m and -200 m and a thin solid contour shows 0 m. (b) Contours from 100 m to 700 m of the first EOF of March mixed layer depth in CCSM3 with thick gray box indicating Labrador Sea Region for box-averaging. (c) Cross-correlation between  $-T$ ,  $S$  and  $\rho$  against mixed layer depth in the thick boxed region shown in the Labrador Sea in (a,b). (d) Cross-correlation between  $-T$ ,  $S$ , and  $\rho$  in the Labrador Sea Region against the MOC index defined in Fig. 1.

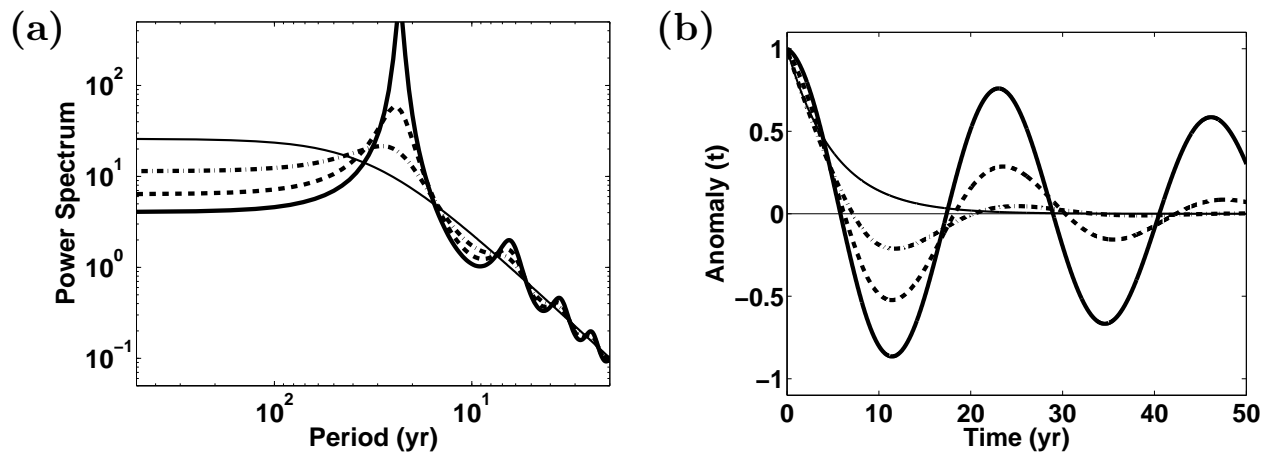


Figure 9: (a) Spectra predicted by the delayed oscillator model in Eq. (4) with parameters  $\alpha = 1$ ,  $t_d = 8$  years,  $\lambda = 2\pi/32$  years $^{-1}$ , and  $D = 0$  (thin solid line),  $D = 0.1$  (dash-dotted,  $q \approx 1$ ),  $D = 0.2$  (dashed,  $q \approx 2.5$ ) and  $D = 0.3$  (thick solid line,  $q \approx 11$ ). (b) “Free solutions” to Eq. (4) as in Czaja and Marshall (2000), see text for details.

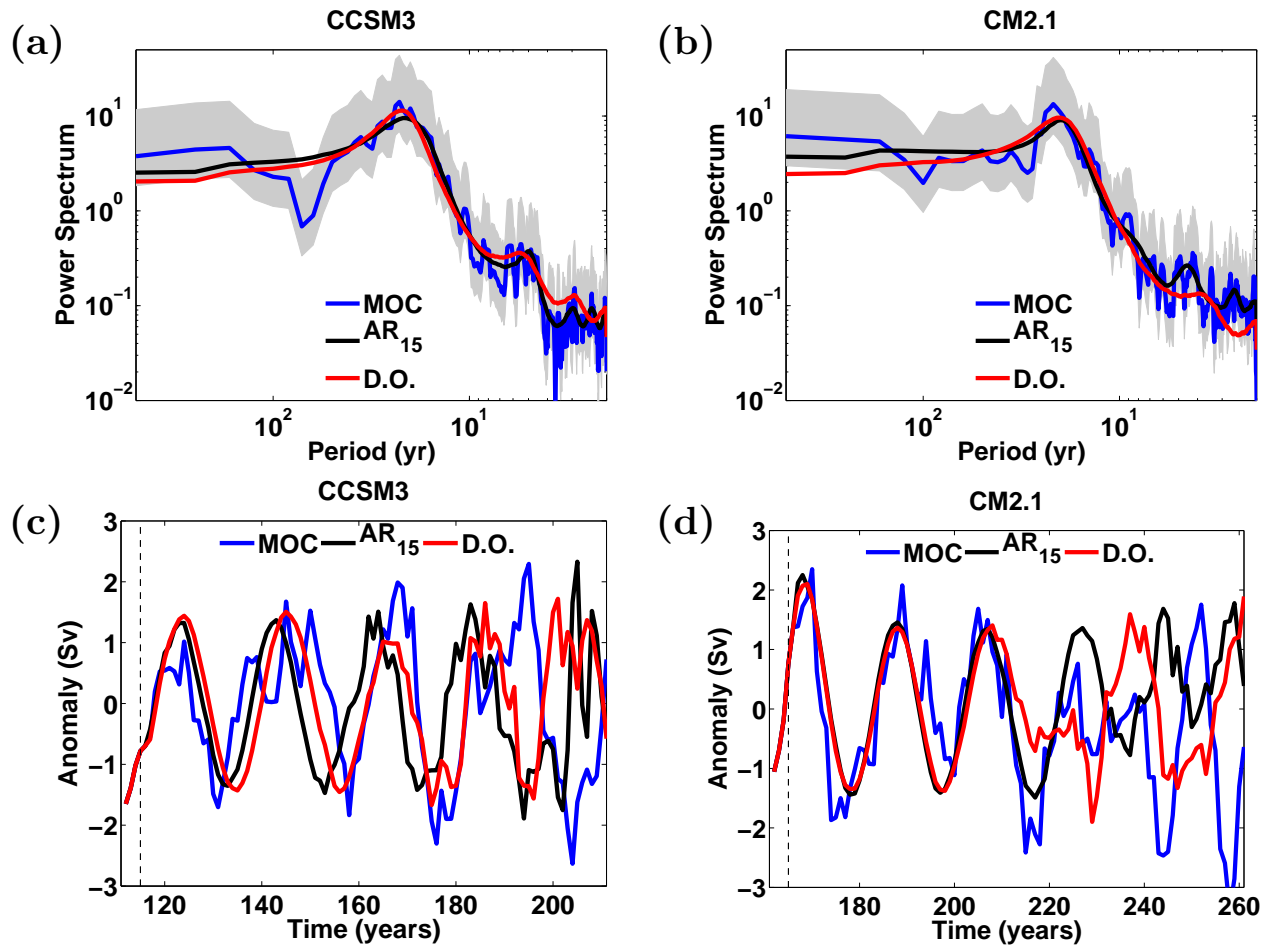


Figure 10: Fit of delayed oscillator models (red lines) to the MOC spectra (blue lines) in (a) CCSM3 and (b) CM2.1. Also plotted in black are spectra of autoregressive ( $AR_{15}$ ) fits to the MOC. Example predictions for the two models are shown in (c,d).



## 570 **Figure Captions**

571 **Figure 1:** (a) Eulerian-mean MOC (in units of Sv) in the Atlantic in CCSM3 and (b) time series of  
 572 the MOC index, defined as the average MOC from 35°N to 50°N and 1800 m to 500 m depth, as  
 573 indicated by the black box in (a). Years marked by x's (squares) denote years that are more than  
 574 one standard deviation above (below) the time mean. These are used to construct composite maps.  
 575 (c) The MOC averaged over years marked by x's minus the MOC averaged over years marked by  
 576 squares, *i.e.*, the MOC(HI)-MOC(LO). The same variables are plotted for CM2.1 in (d), (e) and  
 577 (f).

578 **Figure 2:** (a) Normalized power spectra of the MOC index (red), temperature (K) averaged over  
 579 the top 1 km in the gray-boxed regions shown (b) and (c) (black), and the first principal component  
 580 of temperature (K) in the top 1 km (blue) in CCSM3. The green line indicates a -2 spectral slope  
 581 and the gray shading is a 95% confidence interval. (b) Composite (HI)-(LO) map of temperature  
 582 averaged over the top 1 km, obtained by subtracting the low-index composite from the high-index  
 583 composite, years marked by x's and squares respectively in Fig. 1(b). White shading indicates  
 584 regions that are not significant at the 95% confidence level. (c) First EOF of temperature averaged  
 585 over the top 1 km. The black contour indicates the time-mean zero-wind-stress-curl line. The same  
 586 variables are plotted for CM2.1 in (d), (e), (f), see text for details.

587 **Figure 3:** Composite maps of potential density ( $\text{kg m}^{-3}$ ) averaged over the top 1 km using the  
 588 index described in Fig. 2 for CCSM3. (a) The 5-years-earlier map is obtained by subtracting the  
 589 (low index – 5-years) composite from the (high index – 5-years) composite. (b) As in (a) but at  
 590 the composite index years, (d) as in (a) but 5 years after the composite years, (c) as in (a) but 10  
 591 years after the composite years. Thus, the anomalies evolve in time from the top left to the bottom

592 left. White shading indicates regions that are not significant at the 95% confidence level.

593 **Figure 4:** Same as Fig. 3 but for CM2.1.

594 **Figure 5:** Composite zonal and meridional cross-sections of meridional velocity ( $\text{m}\cdot\text{s}^{-1}$ ) and den-  
 595 sity ( $\text{kg m}^{-3}$ ) in CCSM3 (top row) and CM2.1 (bottom row). The zonal cross-section averaged  
 596 from  $40^\circ\text{N}$  to  $45^\circ\text{N}$  and the meridional cross-section averaged from  $40^\circ\text{W}$  to  $50^\circ\text{W}$  (land points  
 597 were excluded from the zonal mean). Dashed lines in (b) and (e) indicate the extent away from the  
 598 shelf that  $\rho$  was averaged over to compute  $\rho_{WB}$  and  $\rho_{EB}$  (the contribution of  $\rho_{EB}$  in CCSM3 was  
 599 negligible because  $\int_H^0 \rho dz \approx 0$ ) in Fig. 6. White shading indicates regions that are not significant  
 600 at the 95% confidence level.

601 **Figure 6:** (HI)-(LO) index composite mean MOC averaged from  $40^\circ\text{N}$  to  $45^\circ\text{N}$  (solid lines) and  
 602 anomalous streamfunction computed from the composite zonal cross-sections of density (dashed  
 603 lines) in Figs. 5(b) and (e) using Eq. (2). Note that density anomalies on the eastern boundary are  
 604 negligible in CCSM3. See text for details.

605 **Figure 7:** (a) Mean velocity and (b) composite maps of velocity using the index described in Fig. 2  
 606 near 300 m (layer 17) in CCSM3. (c) Mean velocity and (d) composites near 300 m (layer 27) in  
 607 CM2.1. Only vectors significant at the 95% confidence level are shown.

608 **Figure 8:** (a) Contours of March mixed layer depth (m) in CCSM3 using the index described in  
 609 Fig. 2. Thick solid contours are 100 m to 700 m spaced by 100 m, while gray-dotted contours  
 610 show -100 m and -200 m and a thin solid contour shows 0 m. (b) Contours from 100 m to 700 m of  
 611 the first EOF of March mixed layer depth in CCSM3 with thick gray box indicating Labrador Sea  
 612 Region for box-averaging. (c) Cross-correlation between  $-T, S$  and  $\rho$  against mixed layer depth in

613 the thick boxed region shown in the Labrador Sea in (a,b). (d) Cross-correlation between  $-T$ ,  $S$ ,  
 614 and  $\rho$  in the Labrador Sea Region against the MOC index defined in Fig. 1.

615 **Figure 9:** (a) Spectra predicted by the delayed oscillator model in Eq. (4) with parameters  $\alpha = 1$ ,  
 616  $t_d = 8$  years,  $\lambda = 2\pi/32$  years $^{-1}$ , and  $D = 0$  (thin solid line),  $D = 0.1$  (dash-dotted,  $q \approx 1$ ),  
 617  $D = 0.2$  (dashed,  $q \approx 2.5$ ) and  $D = 0.3$  (thick solid line,  $q \approx 11$ ). (b) “Free solutions” to Eq. (4)  
 618 as in Czaja and Marshall (2000), see text for details.

619 **Figure 10:** Fit of delayed oscillator models (red lines) to the MOC spectra (blue lines) in (a)  
 620 CCSM3 and (b) CM2.1. Also plotted in black are spectra of autoregressive ( $AR_{15}$ ) fits to the  
 621 MOC. Example predictions for the two models are shown in (c,d).